

High-speed real-time heterodyne interferometry using software-defined radio

L. M. RIOBO,^{1,2,*} F. E. VEIRAS,^{1,2} M. G. GONZALEZ,^{1,2} M. T. GAREA,¹ AND P. A. SORICETTI¹

¹Universidad de Buenos Aires, Facultad de Ingeniería, Departamento de Física, GLOmAe, Av. Paseo Colón 850, CABA C1063ACV, Argentina

²CONICET, Godoy Cruz 2290 (C1425FQB) CABA, Buenos Aires, Argentina

*Corresponding author: lriobo@conicet.gov.ar

Received 24 August 2017; revised 2 November 2017; accepted 16 November 2017; posted 6 December 2017 (Doc. ID 305548); published 5 January 2018

This paper describes the design and performance of a phase demodulation scheme based on software-defined radio (SDR), applied in heterodyne interferometry. The phase retrieval is performed in real time by means of a low-cost SDR with a wideband optoelectronic front-end. Compared to other demodulation schemes, the system is quite simpler, versatile, and of lower cost. The performance of the demodulator is demonstrated by measuring the displacement per volt of a thin-film polymeric piezoelectric transducer based on polyvinylidene fluoride for ultrasonic applications. We measured displacements between 3.5 μm and 122 μm with 7% relative uncertainty, in the frequency range from 20 kHz to 1 MHz. © 2018 Optical Society of America

OCIS codes: (250.0040) Detectors; (120.3180) Interferometry; (120.4290) Nondestructive testing.

<https://doi.org/10.1364/AO.57.000217>

1. INTRODUCTION

Advanced digital signal processing algorithms greatly improve the performance of real-time heterodyne interferometric systems. Nowadays, signal processing using the software-defined radio (SDR) concept is being applied on systems where versatile and low-cost power-efficient solutions are mandatory. SDR refers to radio communication systems in which almost all of the functionality associated with signal conditioning and processing is digitally implemented. Ideally, the hardware of a SDR system would be limited to an antenna, a high-speed analog-to-digital converter (ADC), and a dedicated processing device. Any demodulation, synchronization, decoding, or decryption required to recover information contained within a received signal would be performed in dedicated software [1]. This system architecture is flexible and may be configured, even in real time, to adapt to various modulation schemes, waveforms, frequency bands, bandwidths, and modes of operation. That is, the SDR is a multi-functional, programmable, and easy to upgrade signal processing system [2]. Present-day SDR implementations allow the designers to focus mostly on the design of the front-end hardware and the processing software, their interfacing, and optimizations for varying system requirements [3].

SDR implementations are the core of new communications paradigms, such as cognitive radio [4] and low-cost transceiver devices [5]. They are used also in optical applications, such as photonic-based coherent radar systems [6] and stabilization of optical frequency combs [7].

In this work we demonstrate a demodulation system for optical heterodyne interferometry based on a low-cost SDR implementation [1,8] and a optoelectronic front-end. We exploit the similarities between optical heterodyne demodulation schemes [9,10] with those used in radio communications systems, to design a high-speed real-time phase demodulator to perform displacement measurement interferometry. The system is applied to the measurement of the electromechanical frequency response of a thin-film polymeric piezoelectric (TPP) transducer based on polyvinylidene fluoride (PVDF).

Our experimental setup consists of a laser light source, a polarization heterodyne interferometer, an optoelectronic front-end, a SDR-based signal processing system, and a personal computer (PC) used for post-processing and display. The interferometer uses a Michelson configuration where the reference and test beams are frequency-shifted by an acousto-optic modulator. A TPP transducer is the device under test (DUT) that undergoes a piezoelectric deformation when excited by a voltage source. The deformation modifies the optical length of one of the interferometer branches and consequently introduces a phase difference between them. To determine the phase difference, we use an optoelectronic front-end that consists of a high-speed photodiode and a transimpedance amplifier, to convert the optical signal into a voltage signal. The voltage signal is conditioned, digitized, and processed by a SDR, which delivers two quadrature digital signals to the output that are post-processed by a PC to retrieve the phase information and, consequently, the deformation of the DUT in real time.

Compared to other demodulation schemes [11–14], this implementation is simpler, more versatile, and of lower cost.

In the following sections, we discuss the detection and demodulation of heterodyne interferometric signals. Then, we describe the operation of the SDR device used in this work, where we use an optical front-end instead of an antenna. The design considerations of the front-end and its performance are then analyzed in detail. Then, we describe the operation principles of the heterodyne interferometer using a SDR device. As an application, we show the experimental results of the measurement of the electromechanical response of a TPP transducer under harmonic excitation, as a function of the applied voltage and frequency on three different points over its surface. Finally, the results of this work are discussed.

2. PHASE DEMODULATION IN HETERODYNE INTERFEROMETRY

There are many demodulation schemes to address phase recovery in heterodyne interferometry. They can be implemented in purely digital systems, analog circuits, or mixed signal processing systems. In the first case, the interferometric signal is digitized directly with a high-speed data acquisition system (such as an oscilloscope), and the samples are processed by means of a dedicated system, such as a PC or a field programmable gate array. Some examples are based on the zero-crossing algorithm [10,15] or the synchroqueezing algorithm [16]. In the analog domain, there are systems based on phase-sensitive detection, such as the phase-locked loop (PLL) [10,17] and quadrature demodulation blocks. In analog systems, the signal from the interferometer is mixed with a reference signal to shift the frequency band of interest to a lower frequency (intermediate frequency) or directly to baseband. Then it is processed with analog circuitry or slower data acquisition systems [11–13,18]. In this section, we describe the output signal from a heterodyne interferometer and the quadrature demodulation algorithm that we will use in our SDR implementation.

The intensity of the optical signal at the output of a heterodyne interferometer can be expressed as

$$I(t) = A + B \cos[2\pi f_c t + p(t)], \quad (1)$$

where A is the background intensity, B is the fringe contrast, f_c is the carrier frequency, and $p(t)$ includes the information and any random phase difference between the branches. The latter may be produced by vibrations or spurious fluctuations of the optical lengths of the arms of the interferometer. From the point of view of telecommunications, Eq. (1) is a phase-modulated signal added to a DC component A . We can rearrange Eq. (1) into

$$I(t) = A + B_I(t) \cos(2\pi f_c t) + B_Q(t) \sin(2\pi f_c t), \quad (2)$$

where

$$B_I(t) = B \cos[p(t)], \quad (3)$$

$$B_Q(t) = -B \sin[p(t)], \quad (4)$$

resembling the structure of quadrature signaling used in telecommunications.

An optoelectronic front-end provides a voltage signal $v(t)$, proportional to $I(t)$ that enters to the quadrature demodulator

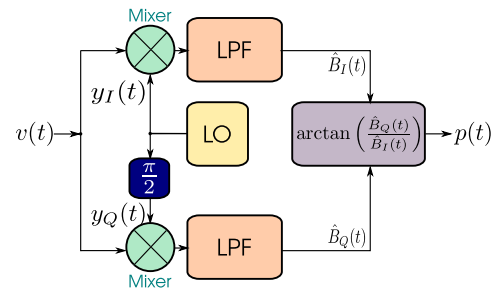


Fig. 1. Quadrature demodulation system. The input signal $v(t)$ is mixed with the reference signals produced by the local oscillator (LO), $y_I(t)$ and $y_Q(t)$, and filtered by low-pass filters (LPF). Both signals are in temporal quadrature.

system described in Fig. 1. The input signal $v(t)$ is mixed with two quadrature signals synthesized by a local oscillator (LO),

$$y_I(t) = K_I \cos(2\pi f_{LO} t), \quad (5)$$

$$y_Q(t) = K_Q \sin(2\pi f_{LO} t), \quad (6)$$

and the high-frequency components at the output of each mixer are low-pass filtered. If $f_{LO} = f_c$, we obtain

$$\hat{B}_I(t) = \frac{BK_I}{2} \cos[p(t)], \quad (7)$$

$$\hat{B}_Q(t) = -\frac{BK_Q}{2} \sin[p(t)]. \quad (8)$$

Finally, if the signals synthesized by the LO have equal amplitudes, from

$$p(t) = \arctan\left(\frac{\hat{B}_Q(t)}{\hat{B}_I(t)}\right) \quad (9)$$

we can retrieve the instantaneous phase, $p(t)$.

The detection process in heterodyne interferometry is less noisy compared to its homodyne counterpart, reaching even the shot noise limit [10,19]. However, the demodulation system in heterodyne interferometry is far more complex than those used in homodyne interferometry. High-frequency design considerations must be carefully attended in the implementations of the optoelectronic front-ends and demodulation systems to avoid high-frequency noise, radiation coupling, and cross talk between subsystems. These requirements make radiofrequency detectors and high-speed subsystems expensive and their design is often geared toward a specific use, reducing their usefulness in different applications. Therefore, the SDR design paradigm was introduced and made it possible to address both issues.

In the next section we describe the working principles of our SDR-based demodulation system and describe how we can use it to demodulate heterodyne interferometric signals.

3. SDR-BASED SIGNAL PROCESSING SYSTEM

Our demodulation system consists of an optoelectronic front-end and a SDR device on which the phase recovery procedure is made in the digital domain by a PC. A picture with the optoelectronic front-end and the SDR is shown in Fig. 2.

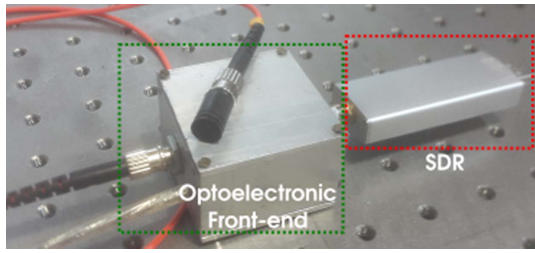


Fig. 2. Picture of the optoelectronic front-end and the SDR device.

A. Optoelectronic Front-End

We designed a wideband optoelectronic front-end to detect the intensity signal from the interferometer [20]. In Fig. 3 the electrical circuit is shown. The circuit consists of a fiber-coupled, high-speed photodiode (Optek OPF482 [21]) and a wideband transimpedance amplifier (TIA) using a junction field-effect transistor input operational amplifier (Texas Instruments OPA657 [22]). The TIA is AC coupled with passive high-pass filters at the input (cutoff frequency: 80 kHz) and at the output (cutoff frequency: 150 kHz). The output impedance is matched to the input impedance of the RTL-SDR.

We use a separate test setup (Fig. 4) to characterize the electrical response of the front-end, in the frequency range from 1 MHz to 200 MHz [20,23]. To test the transimpedance amplifier using a voltage signal generator, we replace the photodiode by its Thevenin electrical representation: a highly valued resistor R_{PH} and its junction capacitance at the applied reverse bias voltage C_{PH} . The magnitude and phase response of the transimpedance amplifier are shown in Fig. 5. The front-end has a cutoff frequency of 140 MHz and has a linear phase response up to 20 MHz. As we described earlier, the front-end is AC coupled to prevent overload and decrease dynamic range. The front-end is enclosed into a metallic box to reduce external

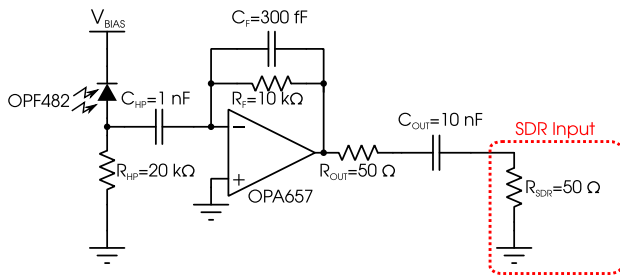


Fig. 3. Schematic circuit of the optoelectronic front-end. The output impedance of the transimpedance amplifier (TIA) is matched to the input impedance of the SDR.

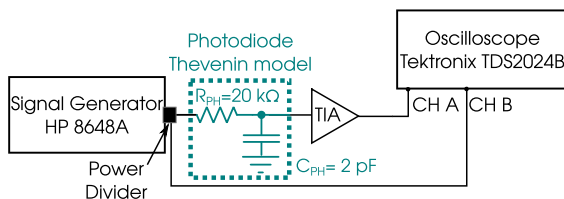


Fig. 4. Experimental scheme used for the characterization of the front-end.

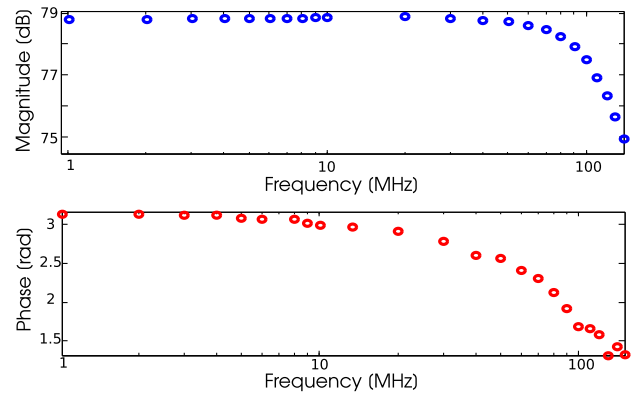


Fig. 5. Magnitude and phase response of the transimpedance amplifier.

coupling of unwanted radio-frequency (RF) signals and the connection to the SDR is made by SubMiniature version A connectors. The power supply of the front-end and the SDR is not shared. This is because the power supply of the SDR is taken from a PC and this supply can be very noisy.

B. SDR Hardware

We use the RTL-SDR as a low-cost universal series bus (USB), software-defined radio device. Originally these devices were designed to be used as digital video broadcast—terrestrial receivers, but it was discovered that they could be used as generic SDRs [1,8].

The RTL-SDR system comprises three stages. The first stage is a RF front-end, usually a 50 Ω antenna, which captures the RF signals and inputs them to the RTL-SDR device. Inside the device, the other two stages are present: an analog signal conditioning and downconversion stage made by a Rafael micro R820T2 circuit [24] and an analog-to-digital conversion and quadrature demodulation stage by a RTL2832U circuit [25]. A block diagram of the entire system is shown in Fig. 6.

Once the RF signal with a carrier frequency f_{IN} is detected by a RF front-end, a voltage signal $v(t)$ enters to the R820T2 circuit, where is amplified by a low-noise amplifier and then bandpass filtered. The output signal mixes with a local oscillator with a frequency f_{LO} that can be configured between 25 MHz and 1.766 GHz. Then it passes through a digitally variable gain amplifier and an anti-alias filter to remove high-frequency products of the mixer. The output signal $v_{IF}(t)$ is proportional to $v(t)$ on which the carrier frequency is shifted to an intermediate frequency $f_{IF} = f_{IN} - f_{LO}$.

The signal $v_{IF}(t)$ enters to the RTL2832U demodulator circuit, on which an ADC converts $v_{IF}(t)$ to a digital signal $v_{IF}(n)$ at a rate $f_S = 28.8$ MHz. This signal is demodulated by a digital quadrature PLL locked to the frequency $N = f_{IF}/f_S$. Two quadrature signals $s_I(n)$ and $s_Q(n)$ are synthesized from a quadrature numerically controlled oscillator and digitally mixed with $v_{IF}(n)$. Each output of the mixers is filtered by finite impulse response decimation filters to remove high-frequency products of the mixing process and reduce the sampling rate of the signals prior to sending them into a data stream to a digital processing system by USB. The sampling rate can be configured, setting the observable bandwidth of the output signal. The maximum stable

sampling rate at the output of the RTL2832U is 2.4 Msamples/s. In this case, we can achieve measurements of the RF spectrum in the frequency range between 25 MHz and 1.766 GHz with a frequency window of 2.4 MHz with 8 bits of resolution.

The test setup to characterize the frequency response of the SDR device is shown in Fig. 7 and the results are in Fig. 8. We analyze the frequency response of the device and test its tuning capability, applying a sinusoid signal with a carrier

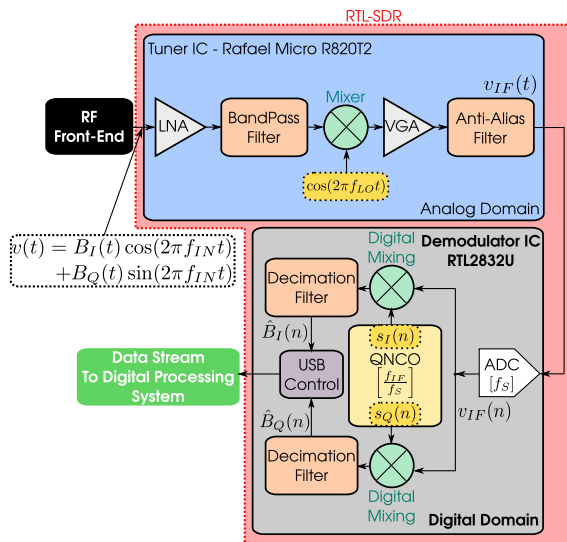


Fig. 6. RTL-SDR system block diagram. LNA, low-noise amplifier; VGA, variable gain amplifier; ADC, analog-to-digital converter; QNCO, quadrature numerically controlled oscillator.

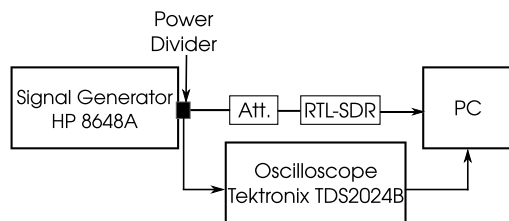


Fig. 7. Experimental scheme used for the characterization of the RTL-SDR device. Att., Attenuator.

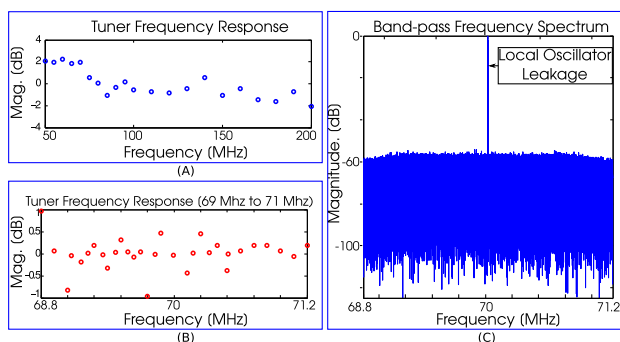


Fig. 8. Frequency response of the RTL-SDR. A: Tuner frequency response. B: Observation bandwidth frequency response. C: Output spectrum of the RTL-SDR (center frequency: 70 MHz). Sampling frequency $F_S = 2.4$ Msamples/s.

frequency in the range from 50 MHz to 200 MHz [Fig. 8A]. The response of the device is flat (on average) with a magnitude deviation of ± 2 dB in the observed range. A closer view of the frequency response is shown in Fig. 8B where the frequency range from 68.8 MHz to 71.2 MHz has a magnitude deviation less than 1 dB. Figure 8C displays a sample of the frequency spectrum reconstructed by the RTL-SDR. As we can see, a part of the local oscillator leaks to the output of the device and must be considered on the demodulation process in further processing. An estimation of the group delay on the frequency window of Fig. 8C was made using a Hilbert-transform-based algorithm [26–28], revealing an average value of -8.4 mrad/Hz between 69 MHz and 71 MHz.

C. Signal Processing Software

The system is controlled with a PC with the open-source software development toolkit GNU Radio, performing also real-time signal processing. GNU Radio applications can be written in either C++ or Python programming language. However, the performance-critical signal processing path is implemented in C++ using processor floating-point extensions. This allow us to implement real-time, high-throughput radio systems in a simple-to-use, rapid-application-development environment [1,29]. In the next section we apply the demodulation system in a heterodyne interferometry system.

4. HETERODYNE INTERFEROMETER USING SOFTWARE-DEFINED RADIO

To test the proposed demodulation system, we use the polarization heterodyne interferometer of Fig. 9. The polarization plane of a linearly polarized He-Ne laser is adjusted by a half-wave plate to ensure that only the polarization normal to the plane of the experiment enters to an acousto-optic modulator (AOM). The AOM is fed by an amplified RF source which drives a sinusoidal voltage signal with a frequency $f_C = 70$ MHz. The AOM is oriented at the Bragg angle to improve the first-order diffraction efficiency. The first-order diffracted beam passes through a polarization beam splitter (PBS) using a fixed mirror, and serves as the reference beam. The zero order serves as the test beam and it is focused on the DUT by means of a microscope objective. A quarter-wave plate is placed in the test arm and it is oriented at 45° from the horizontal plane. Therefore, the test beam traverses it two times.

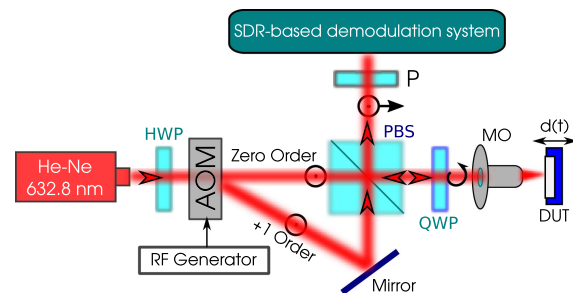


Fig. 9. Heterodyne polarization Michelson interferometer. HWP, half-wave plate; AOM, acousto-optic modulator; PBS, polarized beam splitter; QWP, quarter-wave plate; MO, microscope objective; P , polarizer. $d(t)$ is the DUT off-plane displacement to be measured.

Consequently, the test beam reflected on the sample has its plane of polarization rotated 90° and is recombined with the reference beam by the PBS. Using a polarizer (*P*), we force the interference between the beams, which is detected by the detection block of Fig. 2.

The displacement of the DUT produces an interferometric signal as described in Eq. (2) and, tuning the RTL-SDR to the frequency f_C , the output signals of the demodulator are

$$\hat{B}_I(n) = \frac{BK_I}{2} \cos \left[\frac{4\pi}{\lambda} d(n) + \theta(n) + \Delta\Omega n \right], \quad (10)$$

$$\hat{B}_Q(n) = -\frac{BK_Q}{2} \sin \left[\frac{4\pi}{\lambda} d(n) + \theta(n) + \Delta\Omega n \right], \quad (11)$$

where the term $\theta(n)$ is any random phase difference between the branches of the interferometer, $\Delta\Omega$ is a frequency error that arises from the small difference between the frequency of the acoustic optic modulator, f_C , and the frequency of the local oscillator of the RTL-SDR, f_{LO} . We consider this frequency offset constant in the measurement interval, because all the reference signals in the SDR device are synthesized from a quartz crystal oscillator with a frequency accuracy of ± 1 ppm.

By using the output samples of Eqs. (10) and (11), we can retrieve the phase information with further digital processing. Any mismatches between amplitudes K_I and K_Q are automatically corrected by the RTL-SDR device and by software, so $K_I = K_Q = K$. With these considerations, we can directly apply Eq. (9) and obtain the instantaneous phase:

$$p(n) = \arctan \left(\frac{\hat{B}_Q(n)}{\hat{B}_I(n)} \right) = \frac{4\pi}{\lambda} d(n) + \theta(n) + \Delta\Omega n. \quad (12)$$

As explained above, the term $\Delta\Omega n$ is originated by the frequency mismatch between f_C and f_{LO} and can be easily removed by software.

To validate the proposed method, we measured the electro-mechanical response of a commercial ceramic piezoelectric transducer (Taiwan Piezoceram Technology Corp. PZT TPC-H2518-1.65MR). The results agree very well with those obtained with the setup and method described in a previous article [23]. In the next section we apply the interferometric setup to measure the displacement per unit volt of an ultrasonic TPP transducer.

5. APPLICATION TO THE MEASUREMENT OF THE DISPLACEMENT PER VOLT OF A PVDF TPP TRANSDUCER

PVDF is a widely used semicrystalline polymer with good mechanical properties, resistance to chemicals, high dielectric permittivity, and exceptional pyroelectric and piezoelectric properties [30,31]. Among other uses, thin films of piezoelectric PVDF are of great interest in broadband acoustic and ultrasonic transducers, particularly for medical imaging applications, since they are flexible and with acoustic impedance similar to water and biological tissues [32]. It is well known that quantitative modeling of the frequency response of piezoelectric transducers requires the accurate characterization of the material properties. Compared to inorganic piezoelectric materials, the internal losses (both mechanical and electrical) are much

larger in polymers [33]. In consequence, it is very important to measure the frequency dependence of the electromechanical response for the validation of design models and fabrication of transducers based on piezoelectric polymers [34,35].

Optical interferometric methods allow contact-less, direct measurement of subnanometer dynamic displacements. Unlike other measurement methods as, for example, strain gauge sensors, optical interferometric methods avoid any loading effects that may alter the mechanical properties of the sample. This aspect is particularly interesting in the case of electromechanical properties of piezoelectric polymers.

We characterize the frequency response from 20 kHz to 1 MHz of a TPP transducer based on a 25 μm thick commercial PVDF film (Piezotech Corp.), by measuring the off-plane displacement of the DUT displayed in Fig. 10 with the interferometer shown in Fig. 9. The film is aluminum metalized on both sides, square cut to 16 mm^2 and attached to a double-sided copper-laminated FR4 substrate by means of silver paste. The metallized surfaces are wired to a female BNC connector in order to introduce the excitation voltage.

The DUT is placed over a micrometric displacement stage to measure the mechanical deformation of the sample on three points A, B, and C. Points A and C are on the edges of the sample and point B is on the center. To characterize the displacement of the DUT using a voltage source, we measure the applied voltage and current on the DUT (Stanford Research DS340), so it is possible to calculate the DUT voltage associated with each displacement, as described in [23]. We applied low-amplitude voltages to ensure that the device works in the linear regime. Under this condition, the displacement of the film has a linear relationship with the applied voltage signal.

A typical experimental spectrum retrieved by the RTL-SDR is shown in Fig. 11. A sinusoidal voltage (10 V_{pp} , 500 kHz) is applied to the PVDF film and the displacement of the transducer originates a phase modulation of the optical heterodyne signal at the input of the optoelectronic front-end. The spectrum is viewed directly in real time using a graphical GNU Radio interface.

The spectrum of Fig. 11 reveals all the components present in the interferometric signal in a frequency window of 2.4 MHz around 70 MHz. We choose this value of the carrier signal to avoid any interference from the FM broadcast band. Due to undesirable mechanical vibrations and laser intensity fluctuations,

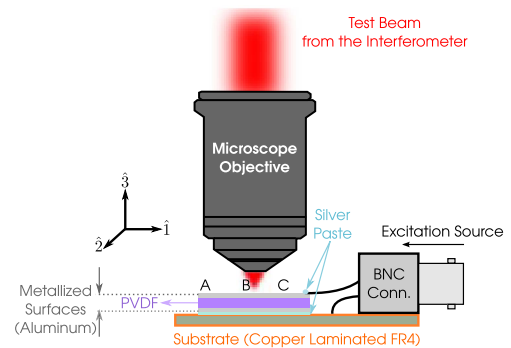


Fig. 10. Sample preparation. The axis of the piezoelectric deformation is shown. A, B, and C are three observation points over the surface of the sample.

the noise is concentrated around the heterodyne carrier component. As we can see, the transducer displacement components [Eq. (2)] are found at 500 kHz from the carrier frequency. This way, a good dynamic range is achieved, more than 40 dB of signal-to-noise ratio (SNR).

In this work, the minimum measured displacement is (3.5 ± 0.2) pm. This corresponds to a 1 MHz sinusoidal excitation ($1 V_{pp}$) at point A. The maximum displacement is (122 ± 10) pm, for a signal amplitude of $10 V_{pp}$ ($f = 120$ kHz) at point B. Low-frequency displacement signals are affected by the noise close to the heterodyne carrier, as shown in Fig. 11. Therefore, the displacement detection limit (i.e., where the SNR = 0 dB) improves from 15 pm at 20 kHz to 0.1 pm at 1 MHz.

To check the linearity of the TPP transducer, the response of the DUT was measured at the three points previously described for different excitation amplitudes. As an example, Fig. 12 shows the experimental data for the DUT at $f = 1$ MHz at excitation amplitudes between 1 and 10 V peak-to-peak. By a linear regression analysis, the displacement per unit volt (i.e., the slope of the displacement as a function of the excitation peak-to-peak voltage), was found to be (4.44 ± 0.35) pm/V at point A,

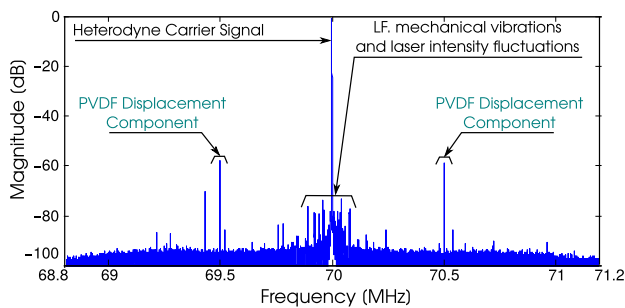


Fig. 11. Spectrum of the interferometric signal. $f_{AOM} = 70$ MHz, $F_S = 2.4$ Msamples/s. DUT voltage: $10 V_{pp}$, DUT frequency: 500 kHz.

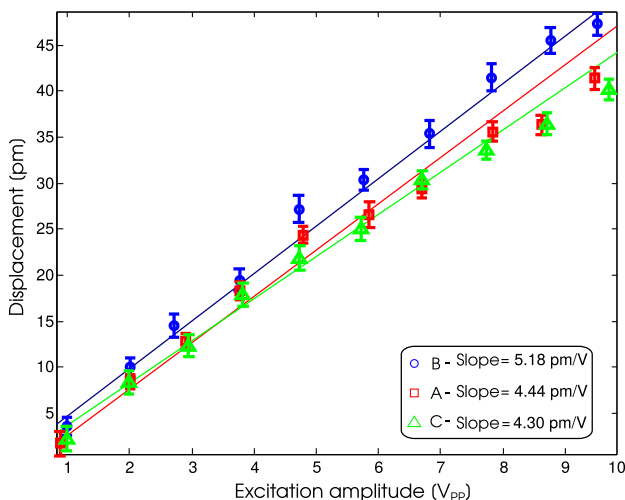


Fig. 12. Displacement versus excitation amplitude at three points of the DUT surface ($f = 1$ MHz). Symbols: experimental data, line: linear regression.

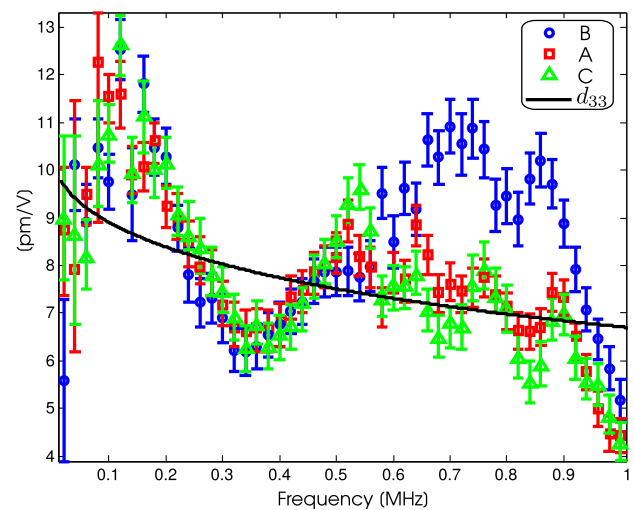


Fig. 13. Electromechanical frequency response of the PVDF transducer in points A, B, and C (symbols with error bars). Piezoelectric coefficient, d_{33} , of a PVDF film (black line, the statistical uncertainty bands are smaller than the linewidth).

(5.18 ± 0.42) pm/V at point B, and (4.30 ± 0.38) pm/V at point C. The determination coefficient (R^2) is better than 0.99 in all cases. The same procedure was carried out in the frequency range from 20 kHz to 1 MHz in steps of 20 kHz to obtain the electromechanical response of the transducer as a function of frequency (Fig. 13). As explained above, low frequency measurements have larger uncertainty due to higher noise levels.

Below 500 kHz, the response of the transducer is essentially the same at the three measurement points (A, B, and C). However, at higher frequencies the response depends on the position. At point B (center of the PVDF film) the displacement per unit volt has a higher value than at the other two points at the edges (that are practically the same). These differences are due to the interaction between higher vibration modes over the surface of the piezoelectric film and in-plane displacements [34,35]. To highlight the difference between the device response and the intrinsic properties of the polymer, in Fig. 13 we also include the piezoelectric coefficient d_{33} , which was measured by an indirect method in a previous article [36]. It can be seen that the electromechanical response of the device (indicated by symbols in Fig. 13) clearly differs from the frequency dependence of the piezoelectric coefficient of the polymer d_{33} (displayed as a continuous line in Fig. 13). As explained above, the transducer displacement per volt depends on the geometry and also includes the effects of the interaction of the piezoelectric polymer with the substrate and other components of the device.

To summarize, the interferometric system described in this work allows the direct measurement of the electromechanical frequency response of the transducer, including its spatial dependence. This is particularly useful for the design and fabrication of TPP transducers.

6. CONCLUSIONS

A high-speed, real-time heterodyne interferometric system is implemented using SDR technology. The flexibility offered

by SDR systems allowed us to focus on the development of the front-end and the signal processing software used for phase recovery. We were able to develop an extremely simple, low-cost, versatile, and compact system using widely available components. The system can be easily adapted to other optical applications where high-speed and real-time data processing are required. The low cost of SDR systems would allow the easy construction and prototyping of detection and demodulation systems for a variety of applications.

A main limitation of the RTL-SDR used in this work is the scarcity of technical documentation, which required a complete characterization of the device. Although its functionality is somewhat limited (since the device was specifically developed for digital video broadcast applications), we were able to measure subnanometer displacements at high frequencies with good signal-to-noise ratio.

The system performance depends on the optical setup (alignment, quality of components, laser power, etc.), the optoelectronic front-end, the SDR characteristics, and the signal processing software. To improve the dynamic range, optical balanced detection schemes can be used [23] together with higher-quality SDR platforms [37–39].

The flexibility of the SDR devices allowed us to simplify the design of the optoelectronic front-end. As described in [20,22,23,40,41], there are numerous trade-offs between gain, noise, and bandwidth. For instance, in this work the high sensitivity of the SDR reduced the gain requirements on the transimpedance amplifier, making it possible to increase its bandwidth.

Since we use an optical interferometric method, we avoid any loading effects that would alter dramatically the mechanical properties of the polymer. Due to the high sensitivity of the demodulation system, we were able to directly measure displacement amplitudes of the order of picometers at frequencies higher than 1 MHz. This made possible to measure the displacement per volt of a PVDF TPP transducer at low excitation voltages (less than 10 V peak-to-peak) in a wide range of frequencies. It should be noted that this essential aspect is of the characterization of transducers.

In future works, we will also use SDR-based systems to study transient phenomena, such as those in optical detection for photoacoustic imaging.

Funding. Universidad de Buenos Aires (UBA) (20020130100346BA, 20020150200143BA, 20020160100042BA, 20020160100052BA); Agencia Nacional de Promoción Científica y Tecnológica (ANPCyT) (PICT 2016-2204).

Acknowledgment. The corresponding author acknowledges a doctoral scholarship from CONICET.

REFERENCES

1. R. W. Stewart, K. W. Barlee, D. S. W. Atkinson, and L. H. Crockett, *Software Defined Radio Using MATLAB & Simulink and the RTL-SDR* (Strathclyde Academic Media, 2015).
2. T. J. Roupheal, *RF and Digital Signal Processing for SDR* (Newnes Newton, 2009).
3. W. Hussain, J. Nurmi, J. Isoaho, and F. Garzia, eds., *Computing Platforms for Software-Defined Radio* (Springer, 2016).
4. H. Sun, A. Nallanathan, C.-X. Wang, and Y. Chen, "Wideband spectrum sensing for cognitive radio networks: a survey," *IEEE Wireless Commun.* **20**, 74–81 (2013).
5. M. Sruthi, M. Abirami, A. Manikoth, R. Gandhiraj, and K. Soman, "Low cost digital transceiver design for software defined radio using RTL-SDR," in *International Multi-Conference on Automation, Computing, Communication, Control and Compressed Sensing (iMac4s)* (IEEE, 2013), pp. 852–855.
6. F. Scotti, F. Laghezza, P. Ghelfi, and A. Bogoni, "Multi-band software-defined coherent radar based on a single photonic transceiver," *IEEE Trans. Microwave Theory Tech.* **63**, 546–552 (2015).
7. M. Čžek, V. Hucl, J. Hrabina, R. Šmd, B. Mikel, J. Lazar, and O. Čp, "Two-stage system based on a software-defined radio for stabilizing of optical frequency combs in long-term experiments," *Sensors* **14**, 1757–1770 (2014).
8. RTL-SDR Blog V3, "RTL-SDR blog V3 datasheet," <http://www.rtl-sdr.com/wp-content/uploads/2017/06/RTL-SDR-Blog-V3-Datasheet.pdf>.
9. P. Hariharan, *Optical Interferometry, Electronics & Electrical* (Academic, 2003).
10. J. D. Ellis, *Field Guide to Displacement Measuring Interferometry* (SPIE, 2014).
11. A. Mlynek, H. Faugel, H. Eixenberger, G. Pautasso, and G. Sellmair, "A simple and versatile phase detector for heterodyne interferometers," *Rev. Sci. Instrum.* **88**, 023504 (2017).
12. M. T. L. Hsu, I. C. M. Littler, D. A. Shaddock, J. Herrmann, R. B. Warrington, and M. B. Gray, "Subpicometer length measurement using heterodyne laser interferometry and all-digital RF phase meters," *Opt. Lett.* **35**, 4202–4204 (2010).
13. C. Wang, Y. Qu, and Y. P. T. Tang, "IQ quadrature demodulation algorithm used in heterodyne detection," *Infrared Phys. Technol.* **72**, 191–194 (2015).
14. K. Delahoussaye, R. Guo, and A. Bhalla, "Homodyne and heterodyne optical interferometry for frequency dependent piezoelectric displacement measurement," *Proc. SPIE* **9200**, 92001M (2014).
15. W. Kokuyama, H. Nozato, A. Ohta, and K. Hattori, "Simple digital phase-measuring algorithm for low-noise heterodyne interferometry," *Meas. Sci. Technol.* **27**, 085001 (2016).
16. A. Bianchetti, F. E. Veiras, P. Etchepareborda, A. L. Vadnjaj, A. Federico, and G. H. Kaufmann, "Amplitude and phase retrieval in simultaneous $\pi/2$ phase-shifting heterodyne interferometry using the synchrosqueezing transform," *Appl. Opt.* **54**, 2132–2140 (2015).
17. P. Bärmann, *Development of a Heterodyne Laser Interferometer for Very Small High Frequency Displacements Detection* (Lund Institute of Technology Department of Atomic Physics, 1992).
18. M. G. González, G. D. Santiago, V. B. Slezak, and A. L. Peuriot, "Simple synchronic detection at audio frequencies through a PC sound card," *Rev. Sci. Instrum.* **78**, 055108 (2007).
19. K. X. Sun, E. K. Gustafson, M. M. Fejer, and R. L. Byer, "Polarization-based balanced heterodyne detection method in a Sagnac interferometer for precision phase measurement," *Opt. Lett.* **22**, 1359–1361 (1997).
20. L. M. Riobo, F. E. Veiras, P. A. Sorichetti, and M. T. Garea, "Wideband transimpedance amplifiers for optoelectronics: applications to dynamic interferometry," *Rev. Elektron.* **1**, 16–19 (2017).
21. Optek Technology, "OPF482 fiber optic detector," <http://uk.farnell.com/optek-technology/opf482/receiver-fibre-optic-to-18-st/dp/1497962>.
22. Texas Instruments, "OPA657 1.6-GHz, low-noise, FET-input operational amplifier," <http://www.ti.com/lit/ds/symlink/opa657.pdf>.
23. L. M. Riobo, F. E. Veiras, P. A. Sorichetti, and M. T. Garea, "Wideband quad optical sensor for high-speed sub-nanometer interferometry," *Appl. Opt.* **56**, 397–403 (2017).
24. Rafael Micro, "Rafael micro R820T2 tuner datasheet," http://www.rtl-sdr.com/wp-content/uploads/2013/04/R820T_datashet-Non_R-20111130_unlocked1.pdf.
25. Realtek, "Rtl2832u: DVB-T COFDM Demodulator+USB 2.0," <http://www.realtek.com.tw/products/productsView.aspx?Langid=1&PFid=35&Level=4&Conn=3&ProdID=257>.
26. S. L. Hahn, *Hilbert Transforms in Signal Processing* (Artech House, 1996), Vol. 2.

27. C. W. Skingle, K. Heron, and D. R. Gaukroger, *The Application of the Hilbert Transform to System Response Analysis* (HM Stationery Office, 1977).
28. F. M. Tesche, "On the use of the Hilbert transform for processing measured CW data," *IEEE Trans. Electromagn. Compat.* **34**, 259–266 (1992).
29. G. Proyect, "Gnu radio," <https://www.gnuradio.org>.
30. M. Broadhurst, G. Davis, J. McKinney, and R. Collins, "Piezoelectricity and pyroelectricity in polyvinylidene fluoride—A model," *J. Appl. Phys.* **49**, 4992–4997 (1978).
31. D. Das-Gupta, "On the nature of pyroelectricity in polyvinylidene fluoride," *Ferroelectrics* **33**, 75–89 (1981).
32. F. S. Foster, K. A. Harasiewicz, and M. D. Sherar, "A history of medical and biological imaging with polyvinylidene fluoride (PVDF) transducers," *IEEE Trans. Ultrason. Ferroelectr. Freq. Control* **47**, 1363–1371 (2000).
33. L. C. Brazzano, P. Sorichetti, G. Santiago, and M. González, "Broadband dielectric characterization of piezoelectric poly(vinylidene fluoride) thin films between 278 k and 308 k," *Polym. Test.* **32**, 1186–1191 (2013).
34. M. G. González, P. A. Sorichetti, and G. D. Santiago, "Modeling thin-film piezoelectric polymer ultrasonic sensors," *Rev. Sci. Instrum.* **85**, 115005 (2014).
35. A. Fernández Vidal, L. Ciocci Brazzano, C. Matteo, P. Sorichetti, and M. González, "Parametric modeling of wideband piezoelectric polymer sensors: design for optoacoustic applications," *Rev. Sci. Instrum.* **88**, 095004 (2017).
36. M. G. González, P. A. Sorichetti, L. C. Brazzano, and G. D. Santiago, "Electromechanical characterization of piezoelectric polymer thin films in a broad frequency range," *Polym. Test.* **37**, 163–169 (2014).
37. M. Richards, "Airsby," in *Radio User* (2015), pp. 8–11.
38. L. Microsystems, "LMS7002M-FPRF MIMO transceiver IC with integrated microcontroller," <http://www.limemicro.com/products/software-defined-radio/>.
39. E. Research, "USRPTM B200mini series," <https://www.ettus.com/product/details/USRP-B200mini>.
40. J. Graeme, *Photodiode Amplifiers: OP AMP Solutions, Gain technology* (McGraw-Hill, 1996).
41. S. Donati, *Electro-Optical Instrumentation: Sensing and Measuring with Lasers* (Pearson Education, 2004).